Multicode Signaling in a Filter Bank Multicarrier Spread Spectrum System and Its Application to HF Communications

**DAVID B. HAAB[1], THOMAS CAMERON SEGO[2], TOM V. HOLSCHUH[2],
HUSSEIN MORADI[2] (Member, IEEE),
AND BEHROUZ FARHANG-BOROUJENY[1] (Life Senior Member, IEEE)**

[1]Electrical and Computer Engineering Department, The University of Utah, Salt Lake City, UT 84112, USA

[2]Spectrum Innovation Department, Idaho National Laboratory, Idaho Falls, ID 83415, USA

CORRESPONDING AUTHOR: B. FARHANG-BOROUJENY (e-mail: farhang@ece.utah.edu).

ABSTRACT The use of filter banks for implementing multicarrier spread spectrum systems leads to a class of effective waveforms that are highly resilient to partial-band interferers. Such waveforms can be also designed to keep the peak-to-average power ratio (PAPR) of the resulting signal at a minimum level. The use of multiple spreading gain vectors (known as multicodes), on the other hand, is an effective method for increasing the data rate in spread spectrum systems, in general. This paper presents a detailed analysis of a class of filter bank multicarrier spread spectrum (FBMC-SS) waveforms and demonstrates an effective receiver implementation of them when multicodes are applied. Application of the developed multicode waveform for communications over high-frequency (HF) skywave channels is also explored, and the benefits that it provides are studied both numerically, through computer simulations, and experimentally, by examining the receivers performance over a variety of skywave links.

INDEX TERMS Filter bank multicarrier, spread spectrum communications, HF communications, multicode methods.

I. INTRODUCTION

DIRECT sequence spread spectrum (DS-SS) and frequency hopping spread spectrum (FH-SS) are two classical spread spectrum methods that were originally developed to establish interference-resistant communications; see [1] and references therein. Multicarrier spread spectrum (MC-SS) systems were proposed later and widely studied in the 1990s; see [2] and references therein. While most of the MC-SS systems make use of the celebrated orthogonal frequency division multiplexing (OFDM) for signal spreading across frequency/subcarriers, a few researchers, [3], [4], [5], have noted that the use of filter banks for signal spreading may lead to a more robust system with higher resistance to partial-band interference.

More recently, our team has revisited the filter bank multicarrier spread spectrum (FBMC-SS) waveform and explored its implementation details, [6], [7]. One particular use case that we have found for the FBMC-SS waveform, with many advantages over the existing waveforms, is communications through high-frequency (HF) skywave channels, [8], where reflections of the electromagnetic waves from layers of ionosphere are used to establish communications over hundreds or thousands of kilometers. In recent years, this method of communications have been found useful for variety of applications, including Internet of Things [9], low-latency communications [10], and many disaster scenarios [11], [12].

One particular feature of HF channels that makes FBMC-SS a perfect match to this application (when compared to other spread spectrum techniques) is the presence of many narrow-band interferers over any band of transmission that is selected. The filter bank's unique ability to isolate portions of the band become instrumental in rejecting such narrow-band interferers without affecting the rest of the spectrum. In addition, low peak-to-average power ratio (PAPR) is another desirable feature that transmit signals in HF modems have to adhere to, given the high-power requirement of the respective

transmitters. The early study of FBMC-SS waveform has shown that effective designs can be applied to keep its PAPR at a low level, [13].

On the other hand, the presence of partial-band interferers along with the fact that typical FBMC-SS signals at the receiver input fall below the thermal noise, makes the task of packet detection and synchronization to an incoming FBMC-SS signal a non-trivial task. Conventional packet detectors, e.g., [14], [15], [16], [17], that rely on standard matched filters perform poorly in such scenarios. Fortunately, the very particular form of FBMC-SS signal construction allows one to develop a modified matched filter that rejects strong interferers blindly while performing the matched filtering operation. The proposed detector that has been named normalized matched filter (NMF) was first presented in [18]. More detailed study of the NMF and its adoption for development of a full receiver structure has been recently presented in [19]. This new implementation that has been named the NMF-based receiver is different from the conventional receivers in previous works [6], [7] that were based on an analysis filter bank (AFB). The results presented in [19] show that the NMF-based receiver, when compared to its AFB counterpart, leads to a reduced complexity and for certain channel conditions may have a superior performance.

Another line of development of FBMC-SS is presented in [20]. In this work, the use of multicodes for increasing the data rate of FBMC-SS has been discussed. The multicodes that have been introduced in this work are chosen such that the low PAPR of the original design of FBMC-SS, [13], is preserved. It should be also noted that the particular form of FBMC that has been mostly adopted by us [6], [7], [18], [19], and others [14], [15], [16], [17], makes use of subcarrier bands that are non-overlapping. This implementation of FBMC is often referred to as filtered multi-tone (FMT), in the broader class of filter bank communications; e.g., see [21]. Taking note of this, in the rest of this paper, we make use of the more specific term FMT-SS (instead of FBMC-SS).

The goal of this paper is to further explore the multicode method of [20] and develop details of the respective receiver structures, following the conventional AFB-based receiver of [6], [7] and the NMF-based receiver that has been recently developed in [19]. More particularly, this paper makes the following contributions:

- A review of FMT-SS that aims at revealing its relevant aspects to the new developments in this paper is presented.
- The multicode method that was first introduced in [20] is further developed, emphasizing on efficient receiver structures for both the AFB-based and NMF-based implementations.
- Complexity analyses of both the AFB-based and NMF-based receivers are presented. This study leads to the finding that the NMF-based receiver offers a lower complexity than that of the AFB-based receiver.

- New simulation results revealing a few less understood performances of the AFB-based and NMF-based receivers and how they compare against one another are presented.
- To validate an application of the developed designs, an extensive set of over-the-air test results over a number of HF skywave links are presented.

The rest of this paper is organized as follows. A brief review of FMT-SS method is presented in Section II. This review includes the FMT-SS signal synthesis, at the transmitter, and methods of signal analysis and information recovery, at the receiver. Some details of the AFB-based and NMF-based receiver that are needed as background for the new developments in the rest of the paper, and are not available in the current publications, are also presented. The multicode method that we first presented in [20] is summarized at the beginning of Section III. The rest of this section is devoted to a number of new developments, including efficient structures for both the AFB-based and NMF-based receivers. A complexity analysis of both the AFB-based and NMF-based receivers is presented in Section IV. Simulation results that compare the two receivers are presented in Section V. Experimental results that we have performed across a broad range of HF skywave links are presented in Section VI and compared against our theoretical and the related simulation results. The concluding remarks of the paper are made in Section VII.

Notations: Our presentation is a mix of continuous-time and discrete-time signals. We use $x(t)$ when reference is made to a continuous-time signal, and $x[n]$ when referring to a discrete-time signal. The signal samples are obtained by making use of a proper synchronization technique, such as the one discussed in [19]. Continuous-time formulations are adopted for presentation of the fundamental concepts and theoretical analysis in Section II and the beginning of Section III. We then switch to discrete-time formulations to provide insight to the detailed implementation of the relevant signal processing algorithms in the remaining parts of the paper. Scalars are upper- and lower-case non-bold letters. Arrays are bold lower-case letters and represented as column vectors. Matrices are bold upper-case letters. The superscripts $(\cdot)^*$, $(\cdot)^T$ and $(\cdot)^H$ represent complex conjugate, transpose, and Hermitian transpose, respectively. Linear convolution is denoted by '$\star$'. The notations $\mathbb{E}[\cdot]$, $\Re[\cdot]$, and $\Im[\cdot]$ refer to the statistical expectation, the real part, and the imaginary part of a variable, respectively. We use $\mathbf{I}$ to denote the identity matrix.
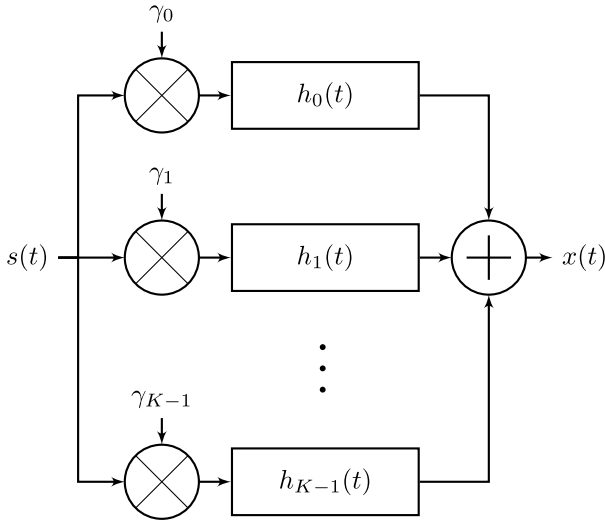
II. REVIEW OF FMT-SS
A. TRANSMITTER
In an FMT-SS system the transmit signal is synthesized as

$$x(t) = s(t) \star g(t). \tag{1}$$

where

$$s(t) = \sum_n s[n]\delta(t - nT), \tag{2}$$

FIGURE 1. FMT-SS transmitter, synthesis filter bank (SFB).

$s[n]$ is the sequence of data symbols, T is the symbol duration, and $g(t)$ is a multi-band pulse-shaping filter expressed as

$$g(t) = \sum_{k=0}^{K-1} \gamma_k h_k(t). \qquad (3)$$

In (3),

$$h_k(t) = h(t) e^{j2\pi f_k t}. \qquad (4)$$

where $h(t)$ is a prototype filter which determines the spectral footprint of each subcarrier. There are K subcarriers, and f_k are the subcarrier center frequencies. Subcarriers are assigned individual complex-valued spreading coefficients γ_k with unit magnitude, i.e., $|\gamma_k| = 1$, and are often optimized for minimizing the PAPR, [13]. Accordingly, the transmit signal (1) is generated using a synthesis filter bank (SFB), as in Fig. 1. It is also worth noting that in FMT the subcarriers center frequencies f_k are chosen such that the filter bank subbands are non-overlapping in the frequency domain, [6].

B. AFB-BASED RECEIVER

In an AFB-based receiver, an estimate of the transmit sequence is generated by passing the received signal through a bank of filters matched to each subcarrier, multiplying each branch by some combining coefficient w_k, and summing all of the branches together, as in Fig. 2. Accordingly, the receiver output is expressed as

$$\hat{s}_{\text{AFB}}(t) = \sum_{k=0}^{K-1} w_k h_k^*(-t) \star y(t). \qquad (5)$$

Here, the combiner coefficients w_k play different roles. First, they undo the phase rotations introduced by the spreading gains γ_k at the transmitter. Second, assuming a flat gain across each subcarrier band, an additional factor equal to the inverse of the respective channel gain is included
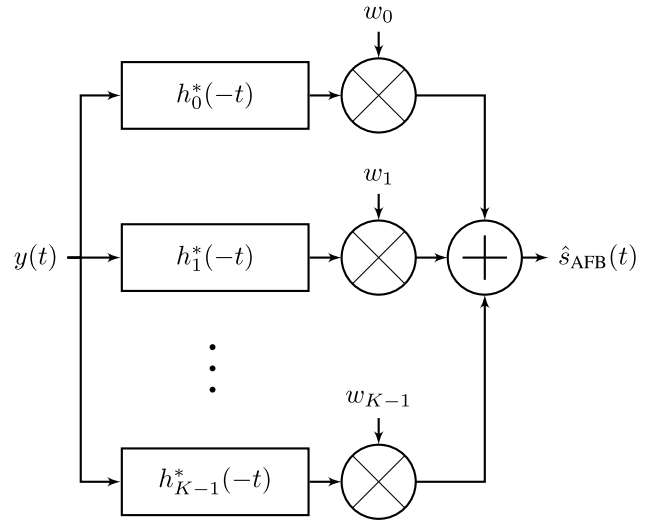
FIGURE 2. FMT-SS receiver, analysis filter bank (AFB).
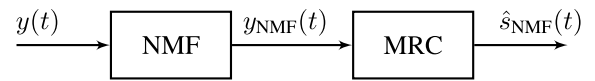
FIGURE 3. NMF-based receiver.

in each coefficient w_k. Moreover, as discussed in [6], the combiner coefficients w_k take into account the signal-to-noise level at each subcarrier and accordingly strike a balance between symbol recovery and noise suppression. Accordingly, the process in (5) is often referred to as maximum ratio combining (MRC); see [6] for details.

Both the transmitter and receiver structures in Figs. 1 and 2, respectively, are implemented efficiently in discrete-time using polyphase structures as in [21, Sec. 5.4-5.5] and [22, Sec. 4.3]. Such implementation, at the receiver, clearly, involves the use of synchronization and channel estimation methods whose details can be found in the literature; e.g., see [19].

C. NMF-BASED RECEIVER

An NFM-based receiver may be divided into two separate parts: (i) NMF part; and (ii) an MRC part. Fig. 3 depicts a block diagram of such a receiver.

Fig. 4 provides the details of the NMF part of Fig. 3. Here, for convenience of explanation, the presentation follows that of an AFB structure, similar to Fig. 2, however, as discussed in [18], a frequency domain implementation may be preferred. As indicated in Fig. 4, the NMF is a cascade of three stages: (i) the AFB; (ii) the power normalization; and (iii) the phase correction and combiner. The AFB stage separates the received signal $y(t)$ into K subcarrier components. In FMT-SS, by design, these subcarrier components belong to mutually exclusive bands, hence, are uncorrelated with one another. The power normalization stage normalizes the signal power in each subcarrier band to unity. At the phase correction and combiner stage, phase corrections are made by removing the phase rotations introduced by the
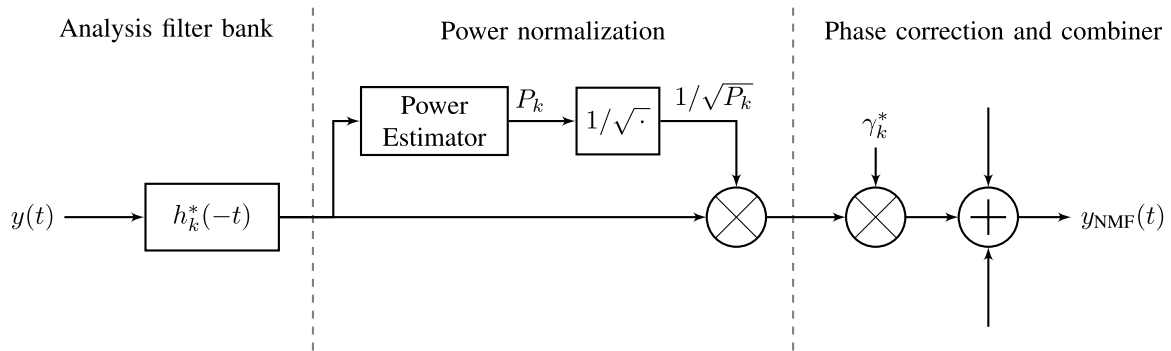
FIGURE 4. Detail of NMF implementation. There are a total of K branches. Only the kth branch is shown here.

spreading factors γ_k, before combining. Alternatively, these phase corrections may be moved to the MRC part of Fig. 3, i.e., absorbed into the MRC coefficients, as in (5).

To understand how NMF works, we first note that if the power normalization blocks are removed from Fig. 4, it implements a standard matched filter of the transmit pulse-shaping filter $g(t)$, viz.,

$$g^*(-t) = \sum_{k=0}^{K-1} \gamma_k^* h_k^*(-t). \tag{6}$$

A key point which helps one in a better understanding of the NMF and parts of the developments in the rest of this paper is an analysis of the combined response of the transmit pulse-shaping filter $g(t)$ and its matched version $g^*(-t)$ at the receiver, i.e.,

$$\eta(t) = g(t) \star g^*(-t). \tag{7}$$

One form of such an analysis has been presented in [6]. In the sequel, we first present a summary of this analysis of [6] and, later, we provide additional interpretations of it that relate to the NMF and multicode method that is presented in the later parts of this paper.

A straightforward analysis of (7), presented in [6], leads to

$$\eta(t) = \beta(t)\rho(t) \tag{8}$$

where $\rho(t) = h(t) \star h(-t)$, by design, is a Nyquist pulse whose peak appears at $t = 0$, and

$$\beta(t) = \sum_{k=0}^{K-1} e^{j2\pi f_k t}. \tag{9}$$

One may notice that $\beta(t)$ is the summation of K complex sine-waves all of the magnitude unity. Hence, the Fourier transform of $\beta(t)$ is effectively a sampled version of a rectangular pulse in the frequency domain, as demonstrated in Fig. 5. In a typical design of the FMT-SS, the pulse-shape $h(t)$ is chosen to be a square-root Nyquist pulse with roll-off factor $\alpha = 1$. Under this condition, the distance between the subcarrier center frequencies f_k is equal to $2/T$; see [6] for the details. This is what we have also assumed here and
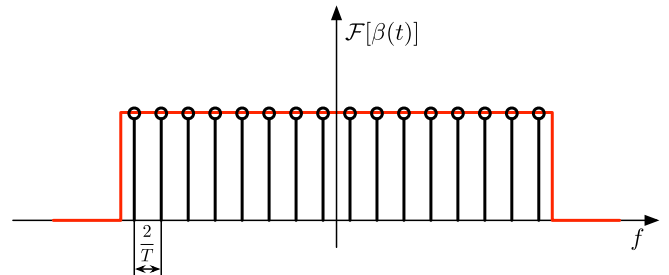

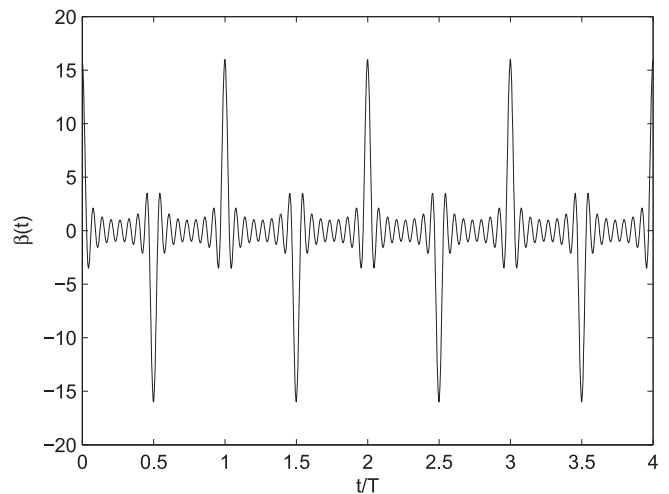**FIGURE 5.** Demonstration of the Fourier transform of $\beta(t)$. Courtesy of [6].

FIGURE 6. An example of $\beta(t)$. Courtesy of [6].

reflected in Fig. 5. This implies that $\beta(t)$ is a train of sinc pulses spaced in time at the interval $T/2$. At $t = 0$ and integer multiples of T, all the components of $\beta(t)$ have zero phase and, thus, add up to the value K. At the points where t is an odd multiple of $T/2$, all the components of $\beta(t)$ have phase of π, thus, add up to the value of $-K$.

An example of $\beta(t)$ for the case where $K = 16$ is presented in Fig. 6. Inserting this result in (7) and taking note that $\rho(t)$ is a Nyquist pulse with the roll-off factor $\alpha = 1$, one will find that, for the present parameters, $\eta(t)$ consists of a sequence of three sinc pulses as shown in Fig. 7.

The presence of a multipath channel $c(t)$, when combined with the transmit pulse-shaping filter $g(t)$ and its matched
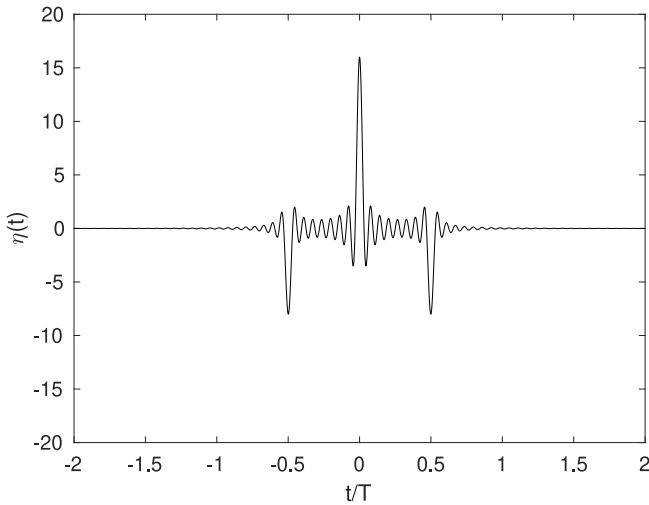
FIGURE 7. An example of $\eta(t)$.

FIGURE 8. The real part of convolution of $g(t)$ with an NMF response.

version $g^*(-t)$ at the receiver, results in an equivalent channel response that may be expressed as

$$c_{\text{eq}}(t) = c(t) \star \eta(t). \tag{10}$$

Accordingly, $c_{\text{eq}}(t)$ replicates multiple copies of $\eta(t)$, each determined by the magnitude and time-delay of the respective path in $c(t)$. An effective receiver should combine the signal energy from these paths to arrive at an optimum/near-optimum detection strategy. One may note that the wider the bandwidth of transmission (equivalently, the larger the number of the subcarriers, K), the narrower the sinc-pulses in $\eta(t)$ will be. This results in a higher resolution in separating the channel multipaths at the matched filter output, hence, leading to a more effective combining of the multipaths and, thus, possibly designing a better detector.

We now divert our attention back to the NMF-based receiver structure in Fig. 3. In the absence of interference and under a high signal-to-noise ratio condition, the normalization stage equalizes the channel at all the subcarriers, assuming a flat gain over each subcarrier band. On the other hand, in a situation where some of the subcarrier bands are affected by some strong interferers, the normalization step suppresses such interferences, leading to an improvement in the receiver performance. To get some insight to the performance of the NMF, here, we present an experiment where the NMF attenuates four out of sixteen subcarrier bands by a set of random gains uniformly distributed in the range 0 to 0.5, while the rest of the subcarrier bands hold the gain of unity. A result of running this experiment is presented in Fig. 8. As seen, the general shape of the matched filter response that we saw in Fig. 7 is preserved here. The observable differences are (i) a reduction in the magnitude of the major pulses (three of them) in the response; and (ii) some random variation in the rest of the response. Obviously, the reduction of the magnitude of the major pulses is a consequence of the fact that some of the sine-wave components in $\beta(t)$ have been attenuated as a result of power normalization. The variation of the side lobes (i.e., the rest of the
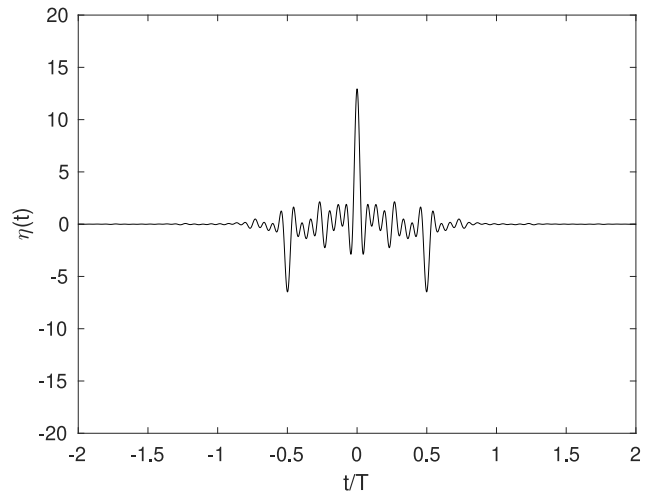
response), on the other hand, is due to the fact that the rectangular function in Fig. 5 is replaced by a distorted one.

III. FMT-SS WITH MULTICODES

The use of multicodes in code division multiple access (CDMA) systems, to increase data rate with little impact on transmit power, is well-known and widely adopted in practice, [23], [24], [25]. This originates and is closely related to the classical method of orthogonal/biorthogonal code modulation, [26].

In the context of FMT-SS modulation, the multicodes may be introduced by taking the following steps. The spreading gain vector $\boldsymbol{\gamma} = [\gamma_0 \ \gamma_1 \ \cdots \ \gamma_{K-1}]^{\text{T}}$ is replaced by a set of orthogonal gain/code vectors $\mathbf{a}_0, \mathbf{a}_1, \cdots, \mathbf{a}_{M-1}$, where M is an integer less than or equal to K. Accordingly, the pulse-shaping filter $g(t)$ varies from symbol-to-symbol and, hence, the transmit signal may be expressed as

$$x(t) = \sum_n s[n]g_n(t) \tag{11}$$

where $g_n(t)$ is from a set of pulse-shapes that vary depending on the selected gain vector. Obviously, compared to the conventional FMT-SS, this construction of the transmit signal allows transmission of more bits per symbol interval, as, in addition to $s[n]$, additional bits may be coded into the selection of the gain vector. For instance, if $s[n]$ is binary and $M = 8$, four (coded) bits will be carried within each symbol interval of the synthesized transmit signal $x(t)$.

Although, in general, $s[n]$ may be chosen from any phase-shift keying (PSK) or quadrature amplitude modulation (QAM) alphabet, in a typical spread spectrum system (including, FMT-SS), $s[n]$ is often limited to binary values. This is because for a detection performance, this allows one to minimize the power spectral density of the transmit signal. For the rest of this paper, we assume that $s[n]$ is binary and is taken from the alphabet $\{+1, -1\}$. With this choice, one may note that blocks of $1 + \log_2 M$ coded bits are mapped to the set of biorthogonal vectors $\{\pm\mathbf{a}_0, \pm\mathbf{a}_1, \ldots, \pm\mathbf{a}_{M-1}\}$.

For this case, the construction of the transmit signal $x(t)$ is named biorthogonal signaling, [26].

A. FMT-SS WITH BIORTHOGONAL SIGNALING

Obviously, there are many choices/variations for the set of orthogonal vectors $\{\mathbf{a}_0, \mathbf{a}_1, \ldots, \mathbf{a}_{M-1}\}$. Among them, a particular choice of interest is the one that minimizes the PAPR of the synthesized signal $x(t)$. The problem of minimization of PAPR in the conventional FMT-SS system, i.e., without multi-coding, has been addressed in [13] and shown how the spreading gains γ_k can be optimized. The optimization algorithm developed in [13] brings down PAPR to a value in the vicinity of 4.5 dB or smaller.

It turns out that a judicious choice of the orthogonal vectors $\{\mathbf{a}_0, \mathbf{a}_1, \ldots, \mathbf{a}_{M-1}\}$ that still preserves the minimum value of PAPR that is reported in [13] exists. This choice that was first reported in [20], sets

$$\mathbf{a}_m = \begin{bmatrix} \gamma_0 e^{j\frac{2\pi m}{K} \times 0} \\ \gamma_1 e^{j\frac{2\pi m}{K} \times 1} \\ \vdots \\ \gamma_{K-1} e^{j\frac{2\pi m}{K} \times (K-1)} \end{bmatrix}, \quad \text{for } 0 \leq m \leq M-1, \quad (12)$$

where the spreading gain parameters γ_0 through γ_{K-1} are those of the conventional FMT-SS and, thus, have been optimized for achieving minimum PAPR.

One may note that the added factors to the gain parameters in (12) are the discrete Fourier transform (DFT) coefficients. Taking note of this and the fact that $|\gamma_k| = 1$, for $k = 0, 1, \ldots, K-1$, it is straightforward to show that

$$\mathbf{a}_m^H \mathbf{a}_{m'} = \begin{cases} K & m' = m \\ 0 & m' \neq m. \end{cases} \quad (13)$$

That is, the vectors $\mathbf{a}_m$ are indeed orthogonal with one another. Next, for completeness of our discussion here, we summarize some of our results from [13] and [20] to explain why the selection of the spreading gain vectors according to (12) preserves the low PAPR of a conventional FMT-SS design.

The key point in minimizing the PAPR in [13] is to first note that $g(t)$ may be factored as

$$g(t) = h(t)\gamma(t) \quad (14)$$

where

$$\gamma(t) = \sum_{k=0}^{K-1} \gamma_k e^{j2\pi f_k t}. \quad (15)$$

It is further noted that since the prototype filter $h(t)$ is a narrowband square-root raised-cosine filter, hence, contains no significant peak, the PAPR of $x(t)$ is dictated by any large peak in $\gamma(t)$. One then may argue that PAPR minimization of $x(t)$ can be achieved by minimizing the crest factor of $\gamma(t)$, for which a solution is reported in [27].

In the case of the synthesized signal $x(t)$ in (11), the pulse-shaping filter $g_n(t)$ varies from symbol to symbol. The pulse-shaping filter $g_n(t)$ are chosen from the set

$$g_{(m)}(t) = h(t)\gamma_{(m)}(t), \quad \text{for } m = 0, 1, \ldots, M-1, \quad (16)$$

where

$$\gamma_{(m)}(t) = \sum_{k=0}^{K-1} \gamma_k e^{j\frac{2\pi km}{K}} e^{j2\pi f_k t}. \quad (17)$$

Noting that in (17), the extra coefficient $e^{j\frac{2\pi km}{K}}$ is effectively a linear phase and the subcarrier frequencies f_k are linearly spaced with a spacing of $2/T$, it is straightforward to show that

$$\gamma_{(m)}(t) = \gamma\left(t + \frac{mT}{2K}\right). \quad (18)$$

That is, for any m, $\gamma_{(m)}(t)$ is a time shifted version of $\gamma(t)$. Hence, it keep the same crest factor and, as a result, no noticeable change in PAPR is observed by switching from a conventional FMT-SS to the one enhanced by multicodes. This point has been confirmed through numerical simulations in [20].

Also, for our future reference, using (13) and recalling that $h(t)$ is a square-root Nyquist filter, one will find that

$$\int_{-\infty}^{\infty} g_{(m)}(t)g_{(m')}^*(-t)dt = \begin{cases} K & m' = m \\ 0 & m' \neq m. \end{cases} \quad (19)$$

Next, we proceed with introducing two difference methods of signal processing steps that are required for the information recovery at the receiver.

B. AFB-BASED RECEIVER

An AFB-based detector/receiver may be constructed by making a modification to the FMT-SS receiver structure in Fig. 2. This modified structure is presented in Fig. 9. Here, the combiner coefficients w_k are set ignoring the DFT coefficients in the spreading gain vectors $\mathbf{a}_0, \mathbf{a}_1, \ldots, \mathbf{a}_{M-1}$. The subsequent IDFT block adds these coefficients and calculates all the outputs hypothesizing that any of the M spreading code vectors has been used. Assuming the spreading gain vector that has been used by the transmitter was $\mathbf{a}_m$, the m'-th output of the IDFT block will be

$$\hat{s}_{m'}[n] = \frac{\sum_{k=0}^{K-1} \frac{|c_k|^2}{\sigma_{v_k}^2} e^{-j\frac{2\pi(m-m')}{K}k}}{\sum_k \frac{|c_k|^2}{\sigma_{v_k}^2}} s[n] + \tilde{v}_m[n] \quad (20)$$

where $\sigma_{v_k}^2$ is the variance of noise plus interference at the kth subcarrier band and $\tilde{v}_m[n]$ is the term arising from the channel noise. The derivation of (20) is straightforward and follows the MRC equations derived in [6].

The decision device in Fig. 9 checks all the values at its input (the outputs of IDFT), finds the one that is closest to $+1$ or -1, and accordingly decides on the spreading gain vector $\mathbf{a}_m$ and the value of $s[n]$, hence, the transmitted bits.
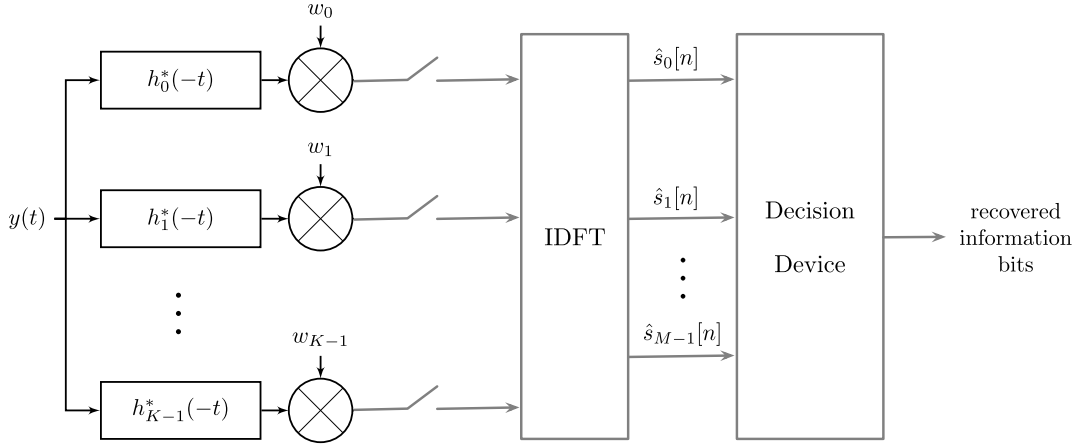
FIGURE 9. AFB-based receiver when biorthogonal signaling in adopted.

C. NMF-BASED RECEIVER

Here, similar to the presentation in Section II-C, we begin with exploring the outcome of passing the received signal through a standard matched filter, i.e., Fig. 4, without the power normalization block. In that case, (7) is replaced by the set of match filtered functions

$$\eta_{(m)}(t) = g_{(m)}(t) \star g^*(-t)$$
$$= \beta_{(m)}(t)\rho(t) \qquad (21)$$

where

$$\beta_{(m)}(t) = \beta\left(t + \frac{mT}{2K}\right). \qquad (22)$$

It should be obvious that due to the time shift $\frac{mT}{2K}$ in (22), here, the positions and the magnitudes of the sinc pulses that were presented in Fig. 7 change dependent on the pulse-shape index m, i.e., the transmitted information bits.

Fig. 10 presents a few examples of $\eta_{(m)}(t)$. Obviously, the receiver can identify the parameter m, hence, the respective information bits, by exploring the positions and magnitudes of the sinc pulses at the matched filter output. Mathematical equations that formalize such detection in an optimal manner is presented in the sequel.

Starting with the transmit signal $x(t)$, in (11), and taking into account the channel response $c(t)$, the output of the NMF may be expressed as

$$x_{\text{NMF}}(t) = \sum_n s[n]\theta_n(t - nT) \star c(t) + v(t) \qquad (23)$$

where $v(t)$ is the term that arises from the channel noise, and

$$\theta_n(t) = g_n(t) \star q(t) \star g^*(-t). \qquad (24)$$

Here, $q(t)$ represents the power normalization part of the NMF; see [19] for details.

Recalling the signal construction (11), one may note that depending on the additional bits transmitted along with the
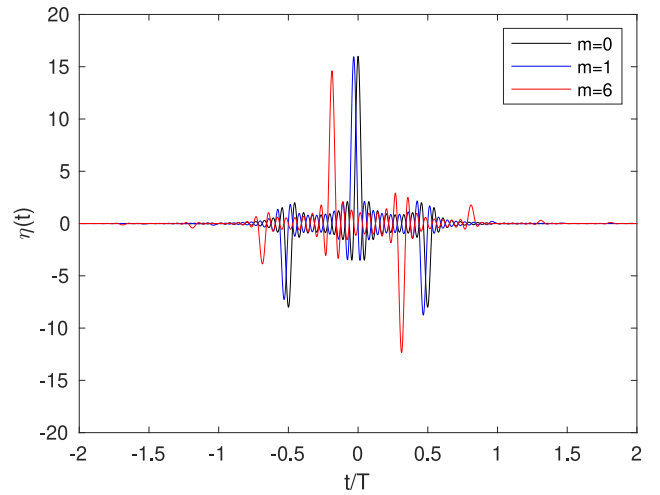

FIGURE 10. A few examples of $\eta_{(m)}(t)$.

data symbol $s[n]$, $\theta_n(t)$ belongs to the pulse-functions set

$$\theta_{(m)}(t) = g_{(m)}(t) \star q(t) \star g^*(-t), \qquad (25)$$

for $m = 0, 1, \ldots, M - 1$.

Next, we note that in a practical implementation, the processing is performed on the signal samples rather than their continuous-time counterparts. We also note that the span of the pulse-functions $\theta_{(m)}(t)$ over time is finite. Such a finite pulse in discrete-time may be represented by a column vector $\boldsymbol{\theta}_{(m)}$ which, following (25), may be expressed as

$$\boldsymbol{\theta}_{(m)} = \mathbf{G}_{\text{SMF}}\mathbf{Q}\mathbf{g}_{(m)} \qquad (26)$$

where $\mathbf{g}_{(m)}$ is column vector of samples of $g_{(m)}(t)$, Q is a convolution matrix for implementing the power normalization step, and $\mathbf{G}_{\text{SMF}}$ is the convolution matrix for implementing the standard matched filter $g^*(-t)$.

With these points in mind, if we concentrate on the samples of $x_{\text{NMF}}(t)$ over the span $\theta_n(t - nT)$ and represent that by the column vector $\mathbf{x}_{\text{NMF}}[n]$, one will find that

$$\mathbf{x}_{\text{NMF}}[n] = s[n]\mathbf{C}\mathbf{G}_{\text{SMF}}\mathbf{Q}\mathbf{g}_n + \mathbf{x}'_{\text{NMF}}[n] + \mathbf{v}[n] \qquad (27)$$

where C is the convolution matrix arising from the samples of the channel response $c(t)$, $\mathbf{x}'_{\text{NMF}}[n]$ represents contributions from the symbols adjacent to $s[n]$, and $\mathbf{v}[n]$ is the noise vector associated with $v(t)$.

To simplify the following derivations, we note that the presence of $\mathbf{x}'_{\text{NMF}}[n]$ in (27) has very little impact on the detection of the information carried by the first term on the right-hand side. This is because both $\mathbf{x}'_{\text{NMF}}[n]$ and the first term are sparse vectors with almost no significant terms in common. With this understanding, $\mathbf{x}'_{\text{NMF}}[n]$ is dropped from (27), and the result is rearranged as

$$\mathbf{x}_{\text{NMF}}[n] = s[n]\mathbf{G}_{\text{SMF}}\mathbf{C}\mathbf{Q}\mathbf{g}_n + \mathbf{G}_{\text{SMF}}\mathbf{w}[n] \quad (28)$$

where in switching the order of $\mathbf{G}_{\text{SMF}}$ and $\mathbf{C}$ we have noted that these are convolutional matrices. Moreover, in (28), $\mathbf{v}[n]$ is replaced by $\mathbf{G}_{\text{SMF}}\mathbf{w}[n]$, where $\mathbf{w}[n]$ is a random vector with independent and identically distributed (i.i.d.) elements. This follows from the fact that, in the NMF, power normalization whitens the channel noise plus interference, leading to a vector $\mathbf{w}[n]$ with i.i.d. elements.

Multiplying (28) through, from left, by the Moore-Penrose pseudo inverse of $\mathbf{G}_{\text{SMF}}$, which is defined as, [28],

$$\mathbf{G}_{\text{SMF}}^+ = \left(\mathbf{G}_{\text{SMF}}^{\text{H}}\mathbf{G}_{\text{SMF}}\right)^{-1}\mathbf{G}_{\text{SMF}}^{\text{H}} \quad (29)$$

we get

$$\begin{aligned}\mathbf{y}_{\text{NMF}}[n] &= \mathbf{G}_{\text{SMF}}^+\mathbf{x}_{\text{NMF}}[n] \\ &= s[n]\mathbf{C}\mathbf{Q}\mathbf{g}_n + \mathbf{w}[n]\end{aligned} \quad (30)$$

Taking note that, in (30), the noise vector $\mathbf{w}[n]$ contains a set of i.i.d. elements, and making use of the dual of (19), i.e., $\mathbf{g}_{(m)}^{\text{H}}\mathbf{g}_{(m')} = K\delta_{mm'}$, one will find that that the following detection rule may be applied

$$\mathbf{g}_{(m)}^{\text{H}}\mathbf{Q}^{\text{H}}\mathbf{C}^{\text{H}}\mathbf{y}_{\text{NMF}}[n] = \begin{cases} \kappa + \mathbf{g}_{(m)}^{\text{H}}\mathbf{Q}^{\text{H}}\mathbf{C}^{\text{H}}\mathbf{w}[n], \\ \quad \text{if } \mathbf{g}_n = \mathbf{g}_{(m)} \\ \mathbf{g}_{(m)}^{\text{H}}\mathbf{Q}^{\text{H}}\mathbf{C}^{\text{H}}\mathbf{w}[n], \\ \quad \text{if } \mathbf{g}_n \neq \pm\mathbf{g}_{(m)} \\ -\kappa + \mathbf{g}_{(m)}^{\text{H}}\mathbf{Q}^{\text{H}}\mathbf{C}^{\text{H}}\mathbf{w}[n], \\ \quad \text{if } \mathbf{g}_n = -\mathbf{g}_{(m)} \end{cases} \quad (31)$$

where $\kappa = \mathbf{g}_{(m)}^{\text{H}}\mathbf{Q}^{\text{H}}\mathbf{C}^{\text{H}}\mathbf{C}\mathbf{Q}\mathbf{g}_{(m)}$. It is not difficult to show that because of the construction of $\mathbf{g}_{(m)}$, κ is independent of the parameter m. Moreover, κ is real and positive.

Following (31), to determine the binary value $s[n]$ and the best match of $\mathbf{g}_n$ to any of the members of the set $\{\mathbf{g}_{(m)}\}$ and, hence, the associated information bits, the detection algorithm presented in Table 1 may be applied.

Next, we take the following steps to simplify the computation of parameter $\kappa_{(m)}$ in Table 1. To this end, we first note that $\mathbf{g}_{(m)}^{\text{H}}\mathbf{Q}^{\text{H}}\mathbf{C}^{\text{H}}\mathbf{y}_{\text{NMF}}[n] = \mathbf{g}_{(m)}^{\text{H}}\mathbf{Q}^{\text{H}}\mathbf{C}^{\text{H}}\mathbf{G}_{\text{SMF}}^+\mathbf{x}_{\text{NMF}}[n]$. Hence, $\kappa_{(m)}$ may be also calculated as

$$\kappa_{(m)} = \Re\left[\mathbf{g}_{(m)}^{\text{H}}\mathbf{Q}^{\text{H}}\mathbf{C}^{\text{H}}\mathbf{G}_{\text{SMF}}^+\mathbf{x}_{\text{NMF}}[n]\right]. \quad (32)$$

We also recall that the matrices $\mathbf{G}_{\text{SMF}}^+$, $\mathbf{C}^{\text{H}}$ and $\mathbf{Q}^{\text{H}}$ have Toeplitz form and when multiplied to a column vector, their

TABLE 1. Detection algorithm of the NMF-based receiver.

for $m = 0 : M - 1$
evaluate $\kappa_{(m)} = \Re\left[\mathbf{g}_{(m)}^{\text{H}}\mathbf{Q}^{\text{H}}\mathbf{C}^{\text{H}}\mathbf{y}_{\text{NMF}}[n]\right]$ and find
the value m that maximizes $|\kappa_{(m)}|$.

The choice of m determines the information bits carried by $\mathbf{g}_n$ and the signum of the associated $\kappa_{(m)}$ gives the value of $s[n]$.

role is to perform a convolution. On the other hand, we note that the pulse-shape vector $\mathbf{g}_{(m)}$ has a limited number of elements at its middle that are significant in amplitude, and the rest converge to zero as they become distant from the center. One may, thus, argue the Toeplitz matrices $\mathbf{G}_{\text{SMF}}^+$, $\mathbf{C}^{\text{H}}$ and $\mathbf{Q}^{\text{H}}$ (after some size adjustment) may be replaced by circulant matrices $\widetilde{\mathbf{G}}_{\text{SMF}}^+$, $\widetilde{\mathbf{C}}^{\text{H}}$ and $\widetilde{\mathbf{Q}}^{\text{H}}$ whose first columns are the same as those of $\mathbf{G}_{\text{SMF}}^+$, $\mathbf{C}^{\text{H}}$ and $\mathbf{Q}^{\text{H}}$, without any significant impact on the calculated value of $\kappa_{(m)}$.

With the above argument, one may choose to evaluate the values of $\kappa_{(m)}$, in Table 1, as

$$\kappa_{(m)} = \Re\left[\mathbf{g}_{(m)}^{\text{H}}\widetilde{\mathbf{Q}}^{\text{H}}\widetilde{\mathbf{C}}^{\text{H}}\widetilde{\mathbf{G}}_{\text{SMF}}^+\mathbf{x}_{\text{NMF}}[n]\right]. \quad (33)$$

We recall that circulant matrices, by definition, are square matrices. Hence, $\widetilde{\mathbf{G}}_{\text{SMF}}^+$, $\widetilde{\mathbf{C}}^{\text{H}}$ and $\widetilde{\mathbf{Q}}^{\text{H}}$ are all of the same size. Obviously, the length of vectors $\mathbf{x}_{\text{NMF}}[n]$ and $\mathbf{g}_{(m)}$ should also match this size. Furthermore, we assume that this size has been selected large enough so that the calculated values of $\kappa_{(m)}$ will be accurate.

Next, we note that circulant matrices are commutable in multiplication. Hence, (33) may be rearranged as

$$\kappa_{(m)} = \Re\left[\mathbf{g}_{(m)}^{\text{H}}\widetilde{\mathbf{G}}_{\text{SMF}}^+\widetilde{\mathbf{Q}}^{\text{H}}\widetilde{\mathbf{C}}^{\text{H}}\mathbf{x}_{\text{NMF}}[n]\right]. \quad (34)$$

Recalling that any circulant matrix $\widetilde{\mathbf{A}}$ can be decomposed as $\widetilde{\mathbf{A}} = \mathcal{F}^{\text{H}}\Lambda_a\mathcal{F}$, where $\mathcal{F}$ is the normalized DFT matrix, such that $\mathcal{F}^{\text{H}}\mathcal{F} = \mathbf{I}$, and Λ_a is a diagonal matrix whose diagonal elements are obtained by taking the DFT of the first column of $\widetilde{\mathbf{A}}$, [29], it is not difficult to show that (34), may be rearranged as

$$\kappa_{(m)} = \Re\left[\mathbf{g}_{(m)}^{\text{H}}\widetilde{\mathbf{G}}_{\text{SMF}}^+\mathcal{F}^{\text{H}}\Lambda_q^{\text{H}}\Lambda_c^{\text{H}}\mathbf{x}_{\text{f,NMF}}[n]\right] \quad (35)$$

where $\mathbf{x}_{\text{f,NMF}}[n] = \mathcal{F}\mathbf{x}_{\text{NMF}}[n]$. The result, here, shows that the matched filtering operation by the channel response and power normalization steps may be added in the frequency domain. Furthermore, taking note that a cost effective implementation of NMF is when it is implemented in the frequency domain, the additions of channel matched filtering and power normalized matched filtering can be performed at a minimum cost.

To continue, we define $\widetilde{\mathbf{x}}_{\text{NMF}}[n] = \mathcal{F}^{\text{H}}\Lambda_q^{\text{H}}\Lambda_c^{\text{H}}\mathbf{x}_{\text{f,NMF}}[n]$, and note that, here, $\widetilde{\mathbf{x}}_{\text{NMF}}[n]$ is the time domain signal vector after adding the channel and power normalized matched filtering to $\mathbf{x}_{\text{NMF}}[n]$. With this definition (35) simplifies to

$$\kappa_{(m)} = \Re\left[\boldsymbol{\varrho}_{(m)}^{\text{H}}\widetilde{\mathbf{x}}_{\text{NMF}}[n]\right]. \quad (36)$$

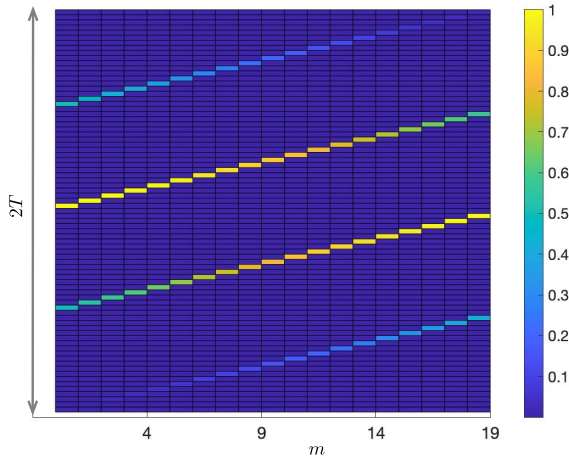**FIGURE 11.** A demonstration of sparsity of a set of vectors $\eta_{(m)} = g_{(m)} \star g_{\text{SMF}}$, for $m = 0, 1, \ldots, M - 1$, and $M = 20$.

where $\varrho_{(m)} = (\widetilde{\mathbf{G}}_{\text{SMF}}^{+})^{\text{H}} \mathbf{g}_{(m)}$. We also note that, here,

$$\widetilde{\mathbf{G}}_{\text{SMF}}^{+} = (\widetilde{\mathbf{G}}_{\text{SMF}}^{\text{H}} \widetilde{\mathbf{G}}_{\text{SMF}})^{-1} \widetilde{\mathbf{G}}_{\text{SMF}}^{\text{H}}$$
$$= \widetilde{\mathbf{G}}_{\text{SMF}}^{-1}. \qquad (37)$$

Hence, one finds that

$$\varrho_{(m)} = \left(\widetilde{\mathbf{G}}_{\text{SMF}}^{-1}\right)^{\text{H}} \mathbf{g}_{(m)}. \qquad (38)$$

Unfortunately, there is an ambiguity in the expression at the right-hand side of (38) that does not allow its direct evaluation. This ambiguity is discussed in the Appendix, at the end of this paper. In the sequel, we proceed with an alternative derivation that lead to a near optimum choice of $\varrho_{(m)}$ without any ambiguity.

Recall that $\widetilde{\mathbf{x}}_{\text{NMF}}[n]$ only covers signal samples originating from the information symbol $s[n]$ and channel noise. The rest of the symbols are included in $\mathbf{x}'_{\text{NMF}}[n]$ which was removed because of the reasons mentioned earlier.

Next, to simplify the analysis and the details that we intend to present here, we assume an ideal channel $c(t) = \delta(t)$ and remove the channel effect (including the channel noise) and apply the standard matched filter to the portion of the transmit signal $s[n]\mathbf{g}_n$. The result will be the signal vector

$$\widetilde{\mathbf{x}}_{\text{SMF}} = s[n](\mathbf{g}_n \star \mathbf{g}_{\text{SMF}}) + (\mathbf{w} \star \mathbf{g}_{\text{SMF}}). \qquad (39)$$

Here, depending on the choice of $\mathbf{g}_n$, the convolution $\mathbf{g}_n \star \mathbf{g}_{\text{SMF}}$ is a member of a set of M vectors that are discrete time versions of the continuous-time functions $\eta_{(m)}(t)$ of (21). As the results in Fig. 10 show, these functions are sparse across time and are non-overlapping. Numerical evaluation of the set of vectors $\eta_{(m)} = \mathbf{g}_{(m)} \star \mathbf{g}_{\text{SMF}}$, for $m = 0, 1, \ldots, M - 1$ reveals that such sparseness also holds for them. Fig. 11 show the magnitudes of a set of vectors $\eta_{(m)}$ for the case where $M = 20$. The fact that these vectors are sparse and non-overlapping across time can be clearly seen in Fig. 11.

The results presented in Fig. 11 reveals the following points:

1) The significant elements of $\eta_{(m)}$ expand over a range of two symbol intervals. This means there may be some inter-symbol interference (ISI) across time over the adjacent symbols.
2) Careful examinations of the results reveal that ISI only occurs when the parameter m is the same for the adjacent symbols. Otherwise, the sparse elements of the vectors $\eta_{(m)}$ do not overlap, hence, no ISI will be present.
3) Considering the observation 2), ISI may be avoided by applying some code design that forces the values of the parameter m to be different across adjacent symbols.

We take note that adding the channel impact and power normalization in NMF will result in some loss of the sparsity of the vectors $\eta_{(m)}$. However, after addition of the matched responses $\mathbf{C}^{\text{H}}$ and $\mathbf{Q}^{\text{H}}$, as specified in (32), most of the sparsity is recovered. We examine the impact of this loss of sparsity numerically through computer simulations later.

Following the observations made above, in the NMF-based receiver, the implementation is completed by taking the following steps.

i) The NMF output samples are calculated and the vector $\mathbf{x}_{\text{NMF}}[n]$ is formed from the samples at the center point of the current symbol, $s[n]$. This vector should cover a duration of $2T$ seconds. Note that, here, $\mathbf{x}_{\text{NMF}}[n]$ is effectively the element of the vector $\widetilde{\mathbf{x}}_{\text{NMF}}[n]$ around its center.
ii) Making use of $\mathbf{x}_{\text{NMF}}[n]$ and correlating with the significant elements of the vectors $\eta_{(m)}$, for $m = 0, 1, \ldots, M - 1$, leads to the decision parameters $\kappa_{(m)}$.
iii) Following the detection algorithm in Table 1, the decision parameters $\kappa_{(m)}$ are used to obtain an estimate of $s[n]$ and the information bits carried by $\mathbf{g}_n$.

Note that, here, the sparsity of the coefficients of $\eta_{(m)}$ is the key point in reducing the complexity of the above implementation.

IV. COMPLEXITY COMPARISONS

Both the AFB-based and NMF-based receivers make use of the NMF and other similar signal processing steps to complete the tasks of packet arrival detection, and carrier and timing synchronization. The task of channel estimation requires the same steps in both receivers. The major difference is the signal processing steps used for information recovery. For this, the AFB-based receiver follows the structure in Fig. 9. This involves an analysis filter bank, an IDFT, and the decision device. The NMF-based receiver, on the other hand, makes use of the NMF that has already been implemented for previous tasks, followed by Steps (ii) and (iii) of the previous section. Step (iii) is effectively the decision device of Fig. 9. Hence, the comparison between the two receiver boils down to comparing Step (ii) of the NMF-based receiver with the AFB followed by the DFT operation in the AFB-based receiver. Given the sparsity of

the coefficients (four of them) that contribute to the evaluation of the decision parameters $\kappa_{(m)}$, one may find that the NMF-based receiver generally has a lower complexity.

V. SIMULATION RESULTS

The performance of both the NMF-based and AFB-based receivers are compared through MATLAB simulations under different HF channel conditions. These simulations begin by generating a discrete-time FMT-SS signal with multicode signaling applied as in Section III-A. Each generated signal contains 1024 random multicode data symbols. The prototype filter $h(t)$ is a square-root raised-cosine pulse-shape with a roll-off factor $\alpha = 1$, truncated to a period of $N = 6$ symbol intervals. The generated transmit signal is then passed through a multipath channel, and an AWGN with the one-sided noise power spectral density N_o is added to the received signal.

Taking note that the signal of interest has a bandwidth of $2K/T_s$ (spanned over the range $-K/T_s < f < K/T_s$), and is sampled at the Nyquist rate $f_{\text{Nyq}} = 2K/T_s$, one finds that the added noise has the power/variance of $\sigma_v^2 = \frac{2K}{T_s}N_o$. Accordingly, the SNR is defined as the ratio of the received signal power (denoted by σ_r^2) over the noise power σ_v^2, viz.,

$$\text{SNR} = \frac{\sigma_r^2}{\sigma_v^2}. \qquad (40)$$

Furthermore, assuming that each multicode symbol carries B bits per symbol, one finds that, here, the energy per bit can be expressed as $E_b = \sigma_r^2 T_s/B$. This leads to the following relationship between SNR and E_b/N_o:

$$E_b/N_o = \frac{2K}{B} \cdot \text{SNR}. \qquad (41)$$

It should be further noted that, here, E_b/N_o is defined at the receiver input, prior to any matched filtering.

Following the original development of FMT-SS for HF skywave channels, [13], we will use the wide-band HF skywave channel model defined in [30] for the presented results. Although it is customary to use the Watterson channel model for narrow-band HF waveform development, [31], the large bandwidth required by FMT-SS necessitates a channel model which adequately describes the behavior of HF channels for wide-band waveforms, i.e., with a higher resolution in the time domain. The channel model of [30] describes a wide-sense stationary uncorrelated scattering (WSSUS) model, where each mode of the channel is modeled by a number of discrete taps. The average power of the channel taps are set such that a specific power-delay profile (PDP) reflecting those of the measured channels are generated. Each channel tap changes randomly over time following a Gaussian stochastic process, i.e., according to a Rayleigh fading model. The reader may refer to [30] for further details.

As noted in [13], there are no standardized channel parameters for modeling the wide-band HF skywave channels. In [32], the suggested channel parameters vary considerably depending on the time of day, ionospheric conditions,

TABLE 2. Simulated model HF channel parameters.

Channel	DT-Q	DT-M	NT-D
Number of modes	1	2	1
Time spread between modes	N/A	T_s	N/A
2σ delay spread of each mode	80 μs	80 μs	615 μs
2σ Doppler spread of each mode	0.1 Hz	0.5 Hz	6.8 Hz
α_r	3	3	3
Δ_r	45 μs	45 μs	360 μs

and latitude of the HF link. Here, we resort to the channel parameters suggested in our previous works pertaining to the measured channels that we had observed, [13], [20]. Minor modifications have been made to better reflect our more recent measured results. We refer to these specific scenarios as (i) day-time "quiet" (DT-Q), (ii) day-time "moderate" (DT-M), and (iii) night-time "disturbed" (NT-D) cases. These cases are summarized in Table 2. The parameters α_r and Δ_r determine the shaping of the channel modes; the reader is directed to [30] for details. One may note that the delay between the modes of the DT-M case is set to the symbol period T_s, to reflect a worst-case ISI scenario.

In line with the previous development of FMT-SS for HF channels, we set the symbol rate to $1/T_s = 1$ kHz. The number of subcarriers is set to $K = 64$. An interfering signal which is 30 dB above this signal level is applied over 1/4 of the subcarrier bands. In the HF skywave domain, the bandwidths of the interfering signals are usually relatively narrow, on the order of 3 kHz, [33], and the interfering signals appear spread out randomly across the whole transmission band. Hence, for the results presented here, the interfering signals are placed over a random set of the subcarriers for each iteration. A RAKE receiver is implemented to take care of the two channel modes in the case of DT-M channel. We have also adopted the symbol scrambling method discussed in [34] to minimize ISI effects. The presented BER curves are generated by averaging the simulated BERs over 1000 independent channel realizations. We assume that the receiver is perfectly synchronized with the received signal both with respect to the carrier frequency and the timing of center of the data symbols. We also assume that the channel is known to the receiver perfectly. This is to mask out the performance losses that incur due to channel state information estimates. The over-the-air (OTA) results that are presented in the next section accounts for these effects.

The simulated BER results of the NMF-based and AFB-based receivers for the DT-Q case are presented in Fig. 12, for the choices of $B = 1$, 2, 4 or 6 bits/symbol. Recall that the case $B = 1$ reduces to BPSK signaling with a single spreading gain vector, i.e., no orthogonal signaling. We observe that the performance of both receivers is identical. A 3 dB loss is present when the number of bits per symbol is increased from 1 to 2, with lower subsequent loss when moving to higher values of B. An alternative method of presenting these results is to plot BERs in terms of E_b/N_o, using (41) for converting SNR to E_b/N_o. Such
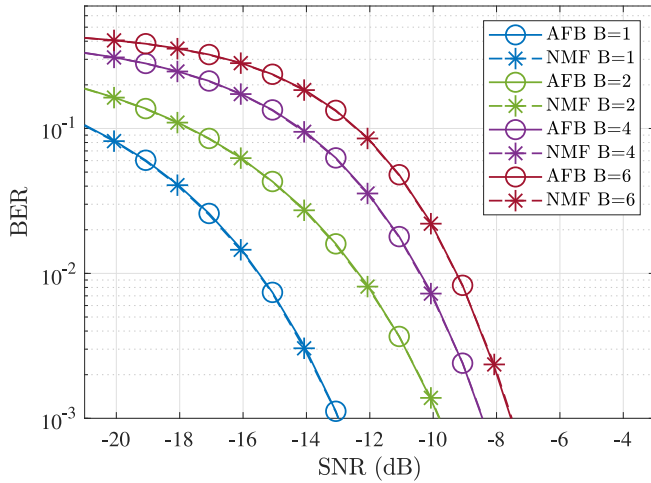
FIGURE 12. BER results of the DT-Q channel.

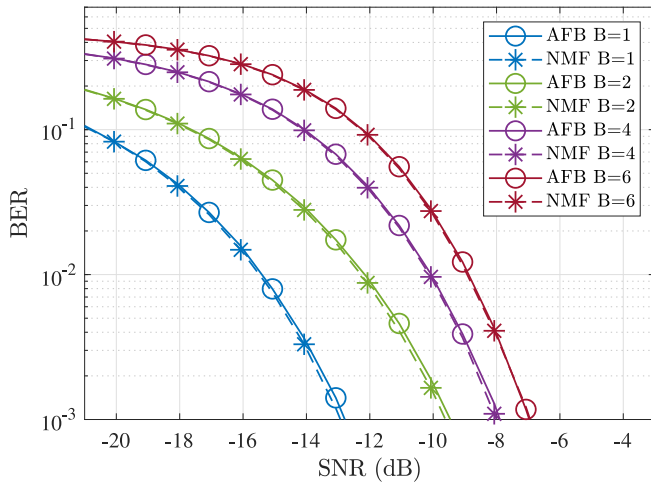**FIGURE 14.** BER results of the NT-D channel.

FIGURE 13. BER results of the DT-M channel.

presentation leads to a set of plots similar to those presented in [26, Fig. 4.4-2], confirming the accurracy of the results in this paper. Here, we have chosen to presents the BERs in terms of SNR, to make the comparisons with the over-the-air results in the next section more convenient and, also, to emphasize on the very low (negative) SNR values that the receiver operates at.

The simulated BER curves for the DT-M case are presented in Fig. 13. These results are very similar to those in Fig. 12. This indicates that the implemented RAKE receivers effectively capture the energies from the two modes of the channel. A fraction of decibel loss, here, is perceived to be due to a small residual ISI between the two modes. This ISI has been minimized by making use of the symbol scrambling method of [34].

Fig. 14 presents BER results for the NT-D channel. The observation here is that while the NMF-based receiver can handle this channel with little loss when compared to the DT-Q channel, the AFB-based receiver incurs 1 dB of loss. This loss is attributed to fact that the NT-D channel has a delay spread that is an order of magnitude larger than those
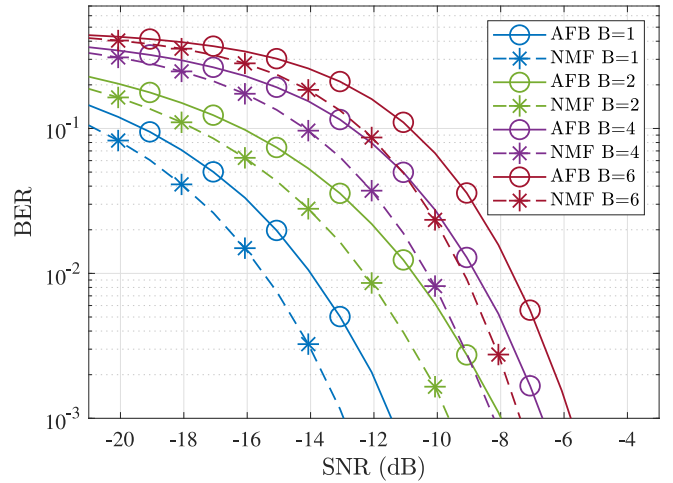
of the DT-Q and DT-M channels; see Table 2. According to the analysis presented in [8], such delay spread is the main source for the performance loss of the AFB-based receiver. The NMF-based receiver, on the other hand, is able to capture the large delay spread of the channel through the channel matched filter, e.g., $\mathbf{C}^{\mathrm{H}}$ in (32).

VI. OVER-THE-AIR EXPERIMENTAL RESULTS

To further verify the performance characteristics of FMT-SS with multicode signaling, a series of test campaigns were conducted. These over-the-air (OTA) tests utilize commercially available off-the-shelf hardware to transmit and receive FMT-SS signals over a number of HF skywave links. The test signals contained known FMT-SS packets with known random data, such that the observed BER for each packet of the demodulated received signal could be recorded. Here, we present a selected set of BER results from these tests for the NMF-based FMT-SS multicode receiver. Note that we omit the results of the AFB-based receiver for brevity, taking note that the results are not much different from those of the NMF-based receiver.

We have examined three HF-skywave links: (i) a short-range link; (ii) a mid-range link; and (iii) a long-range link. A summary of these links, including the date and time of the experiments is presented in Table 3. The BER results of these experiments, over the SNR range −20 to −6 dB, are presented in Figs. 15–17, for short-range, mid-range, and long-range links, respectively. Here, channel estimates are obtained for each packet separately, by making use of the known symbols in the preamble of each packet. Also, channel variation across each packet is tracked through scattered pilots that are inserted after each 7 data symbols. More details of the packet structure that we have used can be found in [34]. Plots are in a form of scattered plots, where each point reflects the results from each packet. Because of insufficient statistics in each packet (carrying a relatively small number of multicode symbols - 1024 symbols, while

TABLE 3. Summary of the examined HF-skywave links.

Link	Transmitter	Receiver	Distance	Date of Experiment
Short-range	Idaho Falls, ID	Salt Lake City, UT	307 km	Dec. 1, 2020
Mid-range	Idaho Falls, ID	Spokane, WA	623 km	Sept. 9, 2021
Long-range	Idaho Falls, ID	Honolulu, HI	4880 km	Nov. 17, 2022
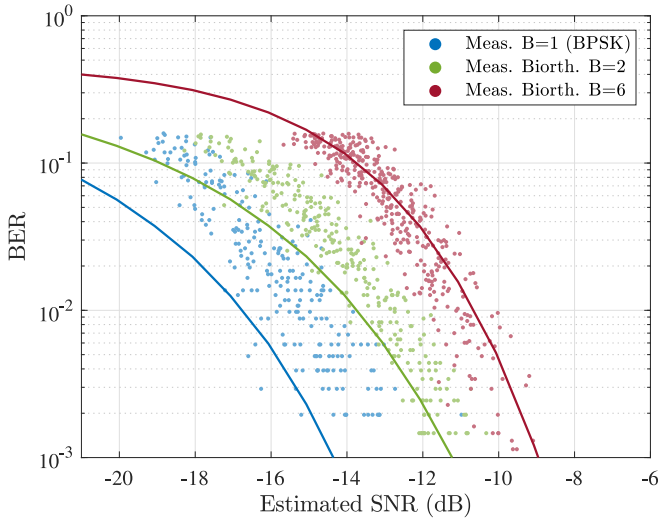
FIGURE 15. Results of Link 1.

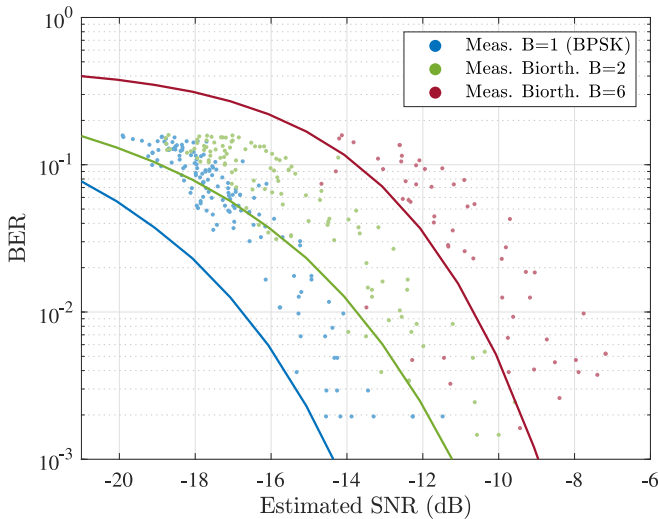**FIGURE 16.** Results of Link 2.

FIGURE 17. Results of Link 3.

looking at BERs of as low as 10^{-3}) and poor channel estimates due to operating at very low SNR values, the BERs are scattered over a relatively wide range.

The full-line plots in Figs. 15–17 are those of the simulated plots, presented in Figs. 12–14. The scattered plots clearly follow the simulated plots, however, due to the additional error introduced by the channel estimation error, some degradation is observed; the average of scattered plots, for most of the results, indicate a shift to right, when compared to the simulated results. Recall that for the simulated results, it was assumed that the channel was known perfectly.
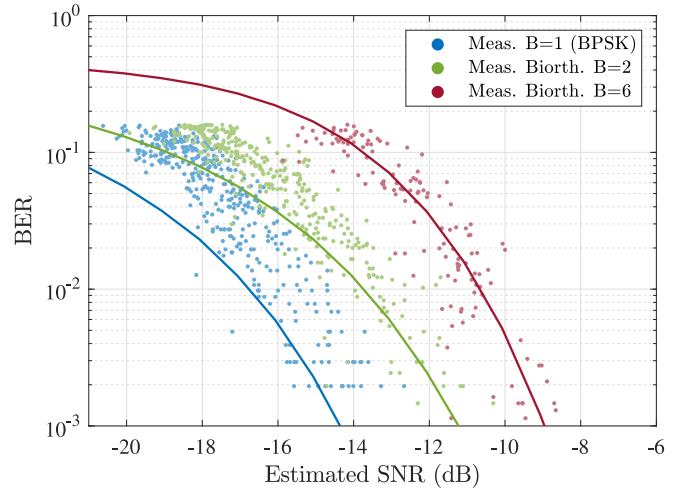
VII. CONCLUSION

This paper presented a detailed analysis and further development of a class of filter bank multicarrier spread spectrum (FBMC-SS) waveforms. The emphasis of the paper was on the use of multicodes for increasing the data rate. The new developments covered detailed implementations of two receiver structures: the AFB-based and NMF-based receivers. We presented methods that minimize the implementation of these two receivers and found that the NMF-based offers a lower complexity. Application of the developed multicode waveform for communications over high-frequency (HF) skywave channels was studied, and the benefits that it provides were explored both numerically, through computer simulations, and experimentally, by examining the receivers performance over a variety of skywave links. From the results presented, we conclude that multicode signaling should be adopted in FBMC-SS systems requiring enhanced data throughput, and that the required changes to the transmitter and receiver structures may be implemented with a reasonable additional cost.

APPENDIX A
COMPUTATIONAL AMBIGUITY OF (38)

We note that the rows of $\widetilde{\mathbf{G}}_{\mathrm{SMF}}$ are circularly shifted copies of the samples $g^*(t)$ (i.e., the time reversed of the standard matched filter $g_{\mathrm{SMF}}(t) = g^*(-t)$), scaled properly while converting from the continuous-time to the discrete-time. We also note that (38) may be rearranged as

$$\varrho_{(m)} = \left(\widetilde{\mathbf{G}}_{\mathrm{SMF}}^{\mathrm{H}}\right)^{-1}\mathbf{g}_{(m)}. \tag{42}$$

Hence, columns of the matrix $\widetilde{\mathbf{G}}_{\mathrm{SMF}}^{\mathrm{H}}$ are the scaled samples of $g(t)$. Similarly, the elements of the vector $\mathbf{g}_{(m)}$ contains scaled samples of $g_{(m)}(t)$. Moreover, recalling (16), one may note that the construction of $\mathbf{g}_{(m)}$ follows the same form as construction of columns of $\widetilde{\mathbf{G}}_{\mathrm{SMF}}^{\mathrm{H}}$ with the difference that the spreading gains γ_k are replaced by $\gamma_k e^{j\frac{2\pi km}{K}}$.

Next, using the identity $\mathbf{A} = \mathcal{F}^{\mathrm{H}} \Lambda_a \mathcal{F}$ that was mentioned earlier (see the text above equation (35)), one will find that (42) may be rearranged as

$$\boldsymbol{\varrho}_{(m)} = \mathcal{F}^{\mathrm{H}} \Lambda_g^{-1} \mathbf{g}_{\mathrm{f},(m)} \tag{43}$$

where $\mathbf{g}_{\mathrm{f},(m)} = \mathcal{F}\mathbf{g}_{(m)}$, i.e., the DFT of $\mathbf{g}_{(m)}$. Also, the diagonal elements of Λ_g are obtained by taking the DFT of the first column of $\widetilde{\mathbf{G}}_{\mathrm{SMF}}^{\mathrm{H}}$. What makes the evaluation of (38) ambiguous, hence, not possible to evaluate, relates to the fact that there are many zeros in both the vector $\mathbf{g}_{\mathrm{f},(m)}$ and the diagonal elements of Λ_g, leading to number of ambiguous zero divide by zero operations.

ACKNOWLEDGMENT

REFERENCES

[1] R. Pickholtz, D. Schilling, and L. Milstein, "Theory of spread-spectrum communications—A tutorial," *IEEE Trans. Commun.*, vol. C-30, no. 5, pp. 855–884, May 1982.

[2] S. Hara and R. Prasad, "Overview of multicarrier CDMA," *IEEE Commun. Mag.*, vol. 35, no. 12, pp. 126–133, Dec. 1997.

[3] S. Kondo and L. B. Milstein, "On the performance of multicarrier DS CDMA systems," *IEEE Trans. Commun.*, vol. 43, no. 12, p. 3101, Dec. 1995.

[4] G. K. Kaleh, "Performance comparison of frequency-diversity and frequency-hopping spread-spectrum systems," *IEEE Trans. Commun.*, vol. 45, no. 8, pp. 910–912, Aug. 1997.

[5] B. Farhang-Boroujeny and C. Furse, "A robust detector for multicarrier spread spectrum transmission over partially jammed channels," *IEEE Trans. Signal Process.*, vol. 53, no. 3, pp. 1038–1044, Mar. 2005.

[6] D. L. Wasden, H. Moradi, and B. Farhang-Boroujeny, "Design and implementation of an underlay control channel for cognitive radios," *IEEE J. Sel. Areas Commun.*, vol. 30, no. 10, pp. 1875–1889, Nov. 2012.

[7] T. Haddadin et al., "An underlay communication channel for 5G cognitive mesh networks: Packet design, implementation, analysis, and experimental results," in *Proc. IEEE Int. Conf. Commun. Workshops (ICC)*, May 2016, pp. 498–504.

[8] S. A. Laraway and B. Farhang-Boroujeny, "Performance analysis of a Multicarrier spread spectrum system in doubly dispersive channels with emphasis on HF communications," *IEEE Open J. Commun. Soc.*, vol. 1, pp. 462–476, 2020.

[9] Y. Li, G. Ding, H. Wang, L. You, and X. Yu, "Cooperative multistation secure transmission in HF Skywave massive MIMO communications for wide-area IoT applications," *IEEE Trans. Rel.*, early access, Jul. 7, 2022, doi: 10.1109/TR.2022.3182665.

[10] T. Arikan and A. C. Singer, "Receiver designs for low-latency HF communications," *IEEE Trans. Wireless Commun.*, vol. 20, no. 5, pp. 3005–3015, May 2021.

[11] J. Wang, G. Ding, and H. Wang, "HF communications: Past, present, and future," *China Commun.*, vol. 15, no. 9, pp. 1–9, 2018.

[12] B. A. Witvliet et al., "Near vertical incidence Skywave propagation: Elevation angles and optimum antenna height for horizontal dipole antennas," *IEEE Antennas Propag. Mag.*, vol. 57, no. 1, pp. 129–146, Feb. 2015.

[13] S. A. Laraway, H. Moradi, and B. Farhang-Boroujeny, "HF band filter bank multi-carrier spread spectrum," in *Proc. IEEE Mil. Commun. Conf. (MILCOM)*, Oct. 2015, pp. 1445–1453.

[14] L. Lampe and K. Witrisal, "Challenges and recent advances in IR-UWB system design," in *Proc. IEEE Int. Symp. Circuits Syst.*, May 2010, pp. 3288–3291.

[15] Q. Zhou, Z. Zou, Q. Chen, H. Tenhunen, and L. Zheng, "Low complexity burst packet detection for wireless-powered UWB RFID systems," in *Proc. IEEE Int. Conf. Ubiquitous Wireless Broadband (ICUWB)*, Oct. 2015, pp. 1–5.

[16] B. Miscopein and J. Schwoerer, "Low complexity synchronization algorithm for non-coherent UWB-IR receivers," in *Proc. IEEE 65th Veh. Technol. Conf. (VTC-Spring)*, Apr. 2007, pp. 2344–2348.

[17] D. Dardari, C. Chong, and M. Win, "Threshold-based time-of-arrival estimators in UWB dense multipath channels," *IEEE Trans. Commun.*, vol. 56, no. 8, pp. 1366–1378, Aug. 2008.

[18] T. Sibbett, H. Moradi, and B. Farhang-Boroujeny, "Normalized matched filter for blind interference suppression," in *Proc. IEEE Mil. Commun. Conf. (MILCOM)*, Oct. 2018, pp. 1–6.

[19] D. B. Haab, H. Moradi, and B. Farhang-Boroujeny, "Spread spectrum symbol detection with blind interference suppression in FBMC-SS," *IEEE Open J. Commun. Soc.*, vol. 2, pp. 1630–1646, 2021.

[20] D. B. Haab, H. Moradi, and B. Farhang-Boroujeny, "Filter bank multi-carrier spread spectrum with biorthogonal signaling for high speed data transmission through HF Skywave channels," in *Proc. IEEE Mil. Commun. Conf. (MILCOM)*, Oct. 2018, pp. 1–9.

[21] B. Farhang-Boroujeny, *Signal Processing Techniques for Software Radios*, 2nd ed. London, U.K.: Lulu, 2010.

[22] P. Vaidyanathan, *Multirate Systems and Filter Banks*. Upper Saddle River, NJ, USA: Prentice-Hall, 1993.

[23] M. A. Abu-Rgheff, *Introduction to CDMA Wireless Communications*. London, U.K.: Academic, Aug. 2007.

[24] *IEEE Standard for Telecommunications and Information Exchange Between Systems—LAN/MAN—Specific Requirements—Part 15: Wireless Medium Access Control (MAC) and Physical Layer (PHY) Specifications for Wireless Personal Area Networks (WPANs)*, IEEE Standard 802.15.1-2002, 2002.

[25] *Guidelines for Using CDMA2000 1x Revision E Features on Earlier Revisions*, 3GPP Standard C.S0099-0, 2011.

[26] J. Proakis and M. Salehi, *Digital Communications*, 5th ed. New York, NY, USA: McGraw-Hill, 2008.

[27] M. Friese, "Multitone signals with low crest factor," *IEEE Trans. Commun.*, vol. 45, no. 10, pp. 1338–1344, Oct. 1997.

[28] R. Penrose, "A generalized inverse for matrices," *Math. Proc. Cambridge Philosoph. Soc.*, vol. 51, no. 3, pp. 406–413, 1955.

[29] R. Gray, *Toeplitz and Circulant Matrices: A Review* (Foundations and Trends in Technology). New York, NY, USA: Now, 2006. [Online]. Available: https://books.google.ca/books?id=PrOi92L5dAUC

[30] J. F. Mastrangelo, J. J. Lemmon, L. E. Vogler, J. A. Hoffmeyer, L. E. Pratt, and C. J. Behm, "A new wideband high frequency channel simulation system," *IEEE Trans. Commun.*, vol. 45, no. 1, pp. 26–34, Jan. 1997.

[31] C. Watterson, J. Juroshek, and W. Bensema, "Experimental confirmation of an HF channel model," *IEEE Trans. Commun. Technol.*, vol. CT-18, no. 6, pp. 792–803, Dec. 1970.

[32] *Testing of HF Modems With Bandwidths of Up to About 12 kHz Using Ionospheric Channel Simulators*, ITU, Geneva, Switzerland, 2010.

[33] E. E. Johnson, E. Koski, W. N. Furman, M. Jorgenson, and J. Nieto, *Third-Generation and Wideband HF Radio Communications*. London, U.K.: Artech House, 2012.

[34] B. T. Hunt, D. B. Haab, T. C. Sego, T. V. Holschuh, H. Moradi, and B. Farhang-Boroujeny, "Examining the performance of MIL-STD-188-110D waveform 0 against FBMC-SS over Skywave HF channels," *IEEE Trans. Veh. Technol.*, vol. 71, no. 11, pp. 11637–11649, Nov. 2022.

DAVID B. HAAB received the B.S. and M.S. degrees in electrical engineering in 2019 and the Ph.D. degree in electrical engineering in 2021 from The University of Utah. Since 2017, he has been working as a Research Assistant with the Wireless Communications Lab, The University of Utah, working in conjunction with Idaho National Laboratory (INL) to develop next-generation radio systems. As of 2022, he works as a Postdoctoral Researcher with The University of Utah in conjunction with INL, Salt Lake City, UT, USA. His research interests include cognitive radio, high frequency skywave communications, multicarrier communications, spread-spectrum waveforms, and software-defined radio implementation.

THOMAS CAMERON SEGO received the B.S. degree in electrical engineering from Utah State University in 2016, and the M.S. degree in electrical and computer engineering from The University of Utah in 2018. Since 2019, He has been working with Idaho National Laboratory as a Wireless Researcher and an Engineer, helping to develop and field next-generation radio devices. He specializes in the implementation of high-frequency radio systems and software-defined radio. His research interests include software-defined radio implementation, spread-spectrum communications, automatic link establishment, and embedded system design.

TOM V. HOLSCHUH is the Manager with the Spectrum Innovation Department. He joined INL in November 2018 after working for DOD for 35 years. He also spent 21 years in the U.S. Army (Special Forces and Military Intelligence), and 14 years as a DOD civilian. He worked at the Office of the Secretary of Defense, Acquisition, Technology and Logistics National Assessment Group for nine years, conducting assessments of capabilities to be fielded to the Special Operations community, ranging from radio frequency jammers, tactical radios and special communications devices to small vessels, and UAVs. Prior to joining INL, he was the Deputy Director for Communications (J6), Special Operations Command Europe for five years.

HUSSEIN MORADI (Member, IEEE) received the bachelor's degree in EE discipline from The University of Texas at Arlington and the master's and Ph.D. degrees in EE discipline from Southern Methodist University, Dallas. He joined Idaho National Laboratory in November 2009. His leadership and technical contributions as a Chief Wireless Scientist and the Technical Director of Spectrum Innovation have been programmatically transformative. He has been issued ten U.S. and foreign patents, plus two additional patents pending. The majority of his patents are for his radio transceiver invention called Wireless Spectrum Communications. This technology is based on Filter-Bank Multi-Carrier Spread Spectrum that can communicate over a range of frequencies while decreasing interference with spectrum sensing technology. It can be leveraged to solve a host of national spectrum sharing challenges including robust communications within congested and contested RF environments while maintaining extremely low-transmission power levels. He was declared "The Inventor of the Year" from 2017 to 2018 by the Idaho National Laboratory and Battelle Energy Alliance. He was the winner of 2012 R&D 100 Awards for his invention. He brings to INL more than 30 years of experience in various elements of corporate R&D leadership. He has been a member of the Board of Professional Engineers since the early 1990's. Prior to joining INL, he assumed lead R&D responsibilities at NEC America, VeriFone, and Kyocera.

BEHROUZ FARHANG-BOROUJENY (Life Senior Member, IEEE) received the B.Sc. degree in electrical engineering from Teheran University, Iran, in 1976, the M.Eng. degree from the University of Wales Institute of Science and Technology, U.K., in 1977, and the Ph.D. degree from the Imperial College, University of London, U.K., in 1981.

From 1981 to 1989, he was with the Isfahan University of Technology, Isfahan, Iran. From 1989 to 2000, he was with the National University of Singapore. Since August 2000, he has been with The University of Utah. He is an expert in the general area of signal processing. In the past, he has worked and has made significant contribution to areas of adaptive filters theory, acoustic echo cancellation, magnetic/optical recoding, and digital subscriber line technologies. His current scientific interests are adaptive filters, multicarrier communications, detection techniques for space-time coded systems, and cognitive radio. He is the author of the books "Adaptive Filters: Theory and Applications," (John Wiley & Sons, 1998), and "Signal Processing Techniques for Software Radio," (self published at Lulu Publishing House, 2009 and 2010, Second Edition). He received the UNESCO Regional Office of Science and Technology for South and Central Asia Young Scientists Award in 1987. He served as an Associate Editor of IEEE TRANSACTIONS ON SIGNAL PROCESSING from July 2002 to July 2005, and IEEE SIGNAL PROCESSING LETTERS from April 2008 to March 2010. He has also been involved in various IEEE activities, including the chairmanship of the Signal Processing/Communications chapter of IEEE of Utah in 2004 and 2005.